

Investigating the $H\alpha$ and [O III] Intensities of HII Regions in M33 with a Focus on NGC 604

Matthew Prem¹, Braden Nowicki¹, Zoe Brunton¹, Saša Maričić¹

¹University of Maryland - College Park

November 19, 2024

1 Abstract

Characterizing nebular emissions provides insight into the physical processes occurring in HII regions (emission nebulae) and, on a larger scale, galaxy formation. We imaged a portion of Messier 33 including NGC 604 – the largest of M33’s emission nebulae – in the $H\alpha$ and [O III] narrowband filters. We employed aperture photometry and edge-detection routines to determine the brightnesses and sizes of NGC 604 and five other HII regions in M33 in both filters. We found NGC 604 appears 3.50 ± 0.17 times brighter and 2.79 ± 0.03 times larger in $H\alpha$ than in [O III]. This is consistent among all analyzed HII regions, which are, on average, 4.08 ± 0.12 times brighter and 3.22 ± 0.06 times larger in the $H\alpha$ filter than in [O III]. These results suggest that similar processes are occurring in NGC 604 and other, smaller star-forming HII regions in M33; these processes result in M33’s emission nebulae appearing brighter and bigger in $H\alpha$ than in [O III].

2 Introduction

The Triangulum Galaxy, Messier 33, is located approximately 2.7 million light-years from Earth and contains over 2,000 emission nebulae, or HII regions (Hodge et al. (1999)), sustained by a recent inflow of gas from the M31-M33 atomic hydrogen bridge (Thilker et al. (2004), Bekki (2008)). M33 is a spiral galaxy much like the Milky Way; as such, characterizing emission HII regions in M33 informs us about the structure and evolution of galaxies similar to our own. We focus on NGC 604 – the largest and most luminous HII region in M33. Since NGC 604 is also the second largest and most luminous star-forming region in the Local Group — and the largest visible from the Northern Hemisphere — it is a valuable case study for exploring the properties of large star-forming regions which were prevalent in the early universe.

Due to recent, intense star formation, NGC 604 has an apparent magnitude of about 12 (Pettit (1954)). The region has a high density of young, massive stars that emit significant amounts of ultraviolet radiation, ionizing the surrounding interstellar gas and producing an emission nebula (Eldridge & Relaño (2011)). The presence of hydrogen and oxygen in these gas clouds suggests the $H\alpha$ (6563 Å) and [O III] (5008 Å) recombination emission lines will be particularly prominent (Freedman et al. (2019)). Since [O III] emissions occur at a shorter wavelength than $H\alpha$ emissions, they require more energy input from the illuminating star to be produced; consequently, we anticipate that [O III] emissions will be found closer to the illuminating star cluster than $H\alpha$ emissions. Additionally, hydrogen is less massive than oxygen and can therefore be more easily dispersed by stellar winds. These factors lead us to expect that the observed nebulae will appear larger in $H\alpha$ filter than [O III], and that they will also exhibit greater brightness in $H\alpha$ due to the higher abundance of atomic hydrogen in the interstellar medium.

To compare the brightness of M33’s HII regions, including NGC 604, we perform aperture photometry on images in the $H\alpha$ and [O III] narrowband filters. Nebulae sizes are obtained via a procedure which iteratively increases the semi-major and semi-minor axes of an ellipse until the increase in brightness is not significantly higher than the sky background. This study aims to determine whether our scientific expectations are supported, thereby providing insight into the complex processes occurring in young, star-forming regions.

3 Observations

All images were taken using the 7-in. AP Refractor Telescope at the University of Maryland, College Park Observatory (field of view: 32×21.5 arcminutes). The 7-in. Refractor uses an SBIG ST-10 Camera set to -15°C . Science images were taken of NGC 604, located at RA 01h 34m 33.79s, DEC $+30^\circ 46' 59''$ (Tabatabaei et al. (2022)). NGC 604’s angular diameter is approximately 1.6 by 1.1 arcminutes – smaller than the field of

view of the 7-in. Refractor. Though the refractor’s field of view is smaller than the angular diameter of M33 – approximately 73 by 45 arcminutes (Nilson (1973)) – the science images still capture other HII Regions in M33 in addition to NGC 604.

All science images were taken with 300 second exposure times in the $H\alpha$ and [O III] narrowband filters. Darks, biases, and flat frames were taken on each observing session. Data were collected over three observing sessions on October 8, 2024, October 17, 2024, and October 27, 2024. The images taken during each observing session are summarized in Tables 1-3.

On October 8, the images were taken by Jasmin Mohammadi and Ava Lee Allen from 18:52 to 22:50 EDT. Transparency was above average, seeing was poor, temperature was in the 59° to 68°F range, and humidity was in the 35% to 40% range.

On October 17, the images were taken by Ryan Tyberg from 18:47 to 23:05 EDT. Transparency was above average, seeing was poor, temperature was in the 50° to 59°F range, and humidity was in the 40% to 45% range. The moon was full or near full.

On October 27, the images were taken by Carol Wilking from 18:47 to 22:45 EDT. Transparency was above average, seeing was average, temperature was in the 41° to 50°F range, and humidity was in the 35% to 45% range.

At the time of year these observations were taken, NGC 604 transited the meridian around local midnight. Since the declination of NGC 604 is only 8.2 degrees less than the latitude of College Park, Maryland, it passes just 8.2 degrees South of the zenith. As a result, the interceding airmass was minimal during the observing sessions.

Image Type	Number of Frames	Target	Exposure Time [s]	Filter
Test	1	NGC 604	300	$H\alpha$
Test	1	NGC 604	120	Clear
Light/Science	10	NGC 604	300	$H\alpha$
Light/Science	10	NGC 604	300	[O III]
Dark	7	N/A	300	N/A
Bias	7	N/A	0	N/A
Flat	7	N/A	15	$H\alpha$
Flat	7	N/A	25	[O III]

Table 1: Images taken on October 8, 2024.

Image Type	Number of Frames	Target	Exposure Time [s]	Filter
Light/Science	13	NGC 604	300	$H\alpha$
Light/Science	13	NGC 604	300	[O III]
Dark	7	N/A	300	N/A
Bias	7	N/A	0	N/A
Flat	8	N/A	15	$H\alpha$
Flat	8	N/A	30	[O III]

Table 2: Images taken on October 17, 2024.

4 Analysis

4.1 Science Image Calibration

Prior to performing scientific analysis, the science images from each data set were calibrated using the bias frames, dark frames, and flat frames from the corresponding data set. This ensures analysis is accurate and increases the precision and signal-to-noise-ratio of each measurement.

4.1.1 Master Bias

Bias images account for additive systematic noise in the CCD in the form of readout noise (excess charges on the CCD) and offset. The bias images were taken as images of zero duration with the shutter closed. Taking

Image Type	Number of Frames	Target	Exposure Time [s]	Filter
Test	1	NGC 604	120	H α
Light/Science	10	NGC 604	300	H α
Light/Science	10	NGC 604	300	[O III]
Dark	7	N/A	300	N/A
Bias	7	N/A	0	N/A
Flat	7	N/A	15	H α
Flat	7	N/A	15	[O III]

Table 3: Images taken on October 27, 2024.

multiple bias images over a short period of time and median combining them into a master bias corrects for the persistent bias pattern of the CCD. The raw bias images from each data set were therefore median combined to produce a master bias for the data set. Figure 1 shows an example master bias. We median combined biases, darks, and flats to eliminate outlier ADU values caused by hot pixels, cosmic rays, and other disturbances.



Figure 1: The calibrated master bias for data from October 27, 2024.

4.1.2 Master Dark

Similarly to bias images, dark images account for additive noise and are taken with the CCD shutter closed; however, they are taken with longer exposure times so charges can collect on the CCD over time. These charges (dark current) are a result of thermal agitation in the silicon crystal lattice of a CCD, and they cannot be ignored for several-minute long exposures if the CCD is not cooled to very low temperatures, around -80° C.

To create a master dark, the master bias was subtracted from each dark image pixel-by-pixel. Then, the calibrated dark images were median combined to form a master dark. The master dark from the third observing session is shown in Figure 2.

4.1.3 Master Flats

Flats account for multiplicative/scaling systematic noise resulting from pixel-to-pixel variations in the quantum efficiency – the percentage of incoming photons absorbed and thus detected by a CCD pixel – of the CCD and non-uniform illumination, which arises from dust and the optics not casting an evenly illuminated image on the

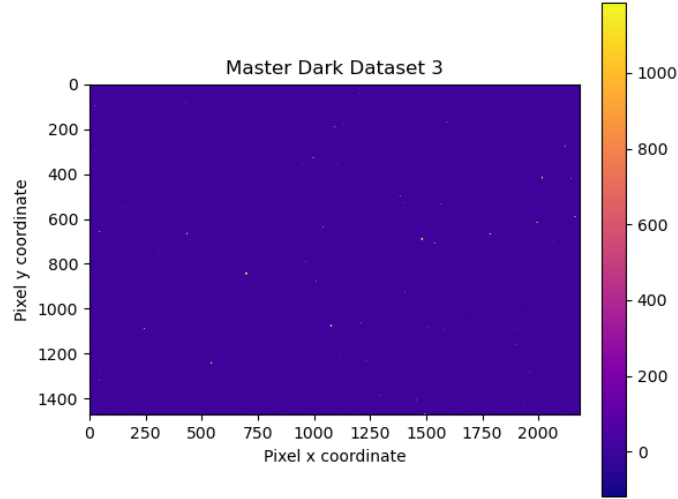


Figure 2: The calibrated master dark for data from October 27, 2024.

CCD. Such variations are different for different filters, so flat frames were taken with both the $H\alpha$ and $[O III]$ narrowband filters. To detect variation, the flat fields were taken towards an ideally uniformly illuminated white surface in the observatory.

To produce a master flat, the master bias and master dark were subtracted from each raw flat image. The master dark was scaled by the ratio of the flat frame exposure time to the dark frame exposure time before subtracting. Here, we make the approximation that dark current accumulates linearly with time, so the dark frame is simply scaled by the ratio of exposure times.

We then median combined these calibrated flat frames into master flats in each filter. Since flats account for multiplicative noise, we ultimately divide the master flat from the science images. We care about variation among pixels, not the exact flat ADU values; additionally, ADU values are typically very high in flat images, so dividing the values from our science images would drown out our science data. Instead, we normalized the master flat, dividing it by the median of the master flat frame. If we normalized with the max value, we could normalize with a hot pixel, which would disturb our results. The $H\alpha$ master flat from the third observing session is shown in Figure 3.

4.1.4 Calibrating Science Images

With a master bias, master dark, and normalized master flats, we calibrated each science image to obtain an (ideally) true image. For each science image, we subtracted the master bias and subtract the master dark scaled by the ratio of the science frame exposure time to the dark frame exposure time. We then divided the bias- and dark-subtracted light frame by the normalized master flat frame taken with the same filter as the light frame. All of these operations are done pixel-by-pixel.

An equation representing this science image calibration is

$$S_{\lambda}^*[x, y] = \frac{S_{\lambda}[x, y] - \left(\frac{t_S}{t_D}\right) D[x, y] - B[x, y]}{F_{\lambda}^n[x, y]} \quad (1)$$

where $S_{\lambda}^*[x, y]$ is the calibrated science image taken at a certain wavelength or wavelength range (in this case, associated with the B filter), $S_{\lambda}[x, y]$ is the raw science frame, t_S is the science frame exposure time, t_D is the dark frame exposure time, $D[x, y]$ is the master dark, $B[x, y]$ is the master bias, and $F_{\lambda}^n[x, y]$ is the normalized master flat associated with the same wavelength range or filter as the science image. The $[x, y]$ indicate that these operations are done on each pixel, marked by coordinates in a two-dimensional array.

4.1.5 Aligning and Co-Adding Science Images

We co-added all of the calibrated science images to increase the signal-to-noise ratio for later analysis. Before co-adding, we aligned the science images in each data set using a bright-star comparison procedure. A bright star

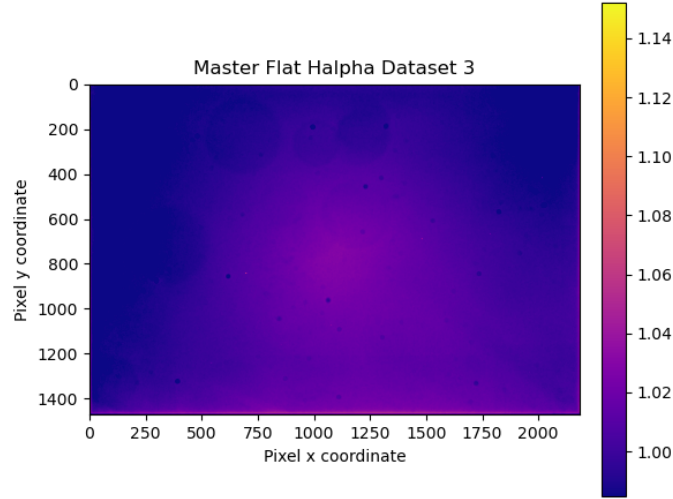


Figure 3: The calibrated $H\alpha$ master flat for data from October 27, 2024.

was selected in an image. In each subsequent image, we find the pixel coordinates of the brightest pixel within a region around the coordinates of the selected comparison star and shift the new image to align the bright pixels of both images. All images are shifted to correspond with the first image.

We then co-added the images, adding ADU values pixel-by-pixel, to make a combined, calibrated science image from each data set. The alignment and co-adding process was performed on the calibrated science images in each dataset, resulting in three science images in each filter, along with master calibration frames used. The three images in each filter were aligned using the same alignment procedure. A second star was selected to determine relative rotation angles between each image, and the images were rotated as necessary for proper alignment. The science images from each dataset were then co-added, producing a final image in $H\alpha$ and an image in $[O III]$ for photometric analysis. The calibrated science images in $H\alpha$ and $[O III]$ from the third observing session are shown in Figure 4. Figures 5 and 6 give the combined science images from all three datasets.

4.2 Brightness Analysis: Aperture Photometry

We identified the pixel positions of six nebulae, including NGC 604, in the $H\alpha$ and $[O III]$ images. The nebulae under consideration and their locations are listed in Table 4. NGC 604 and NGC 595 are named; nebulae which

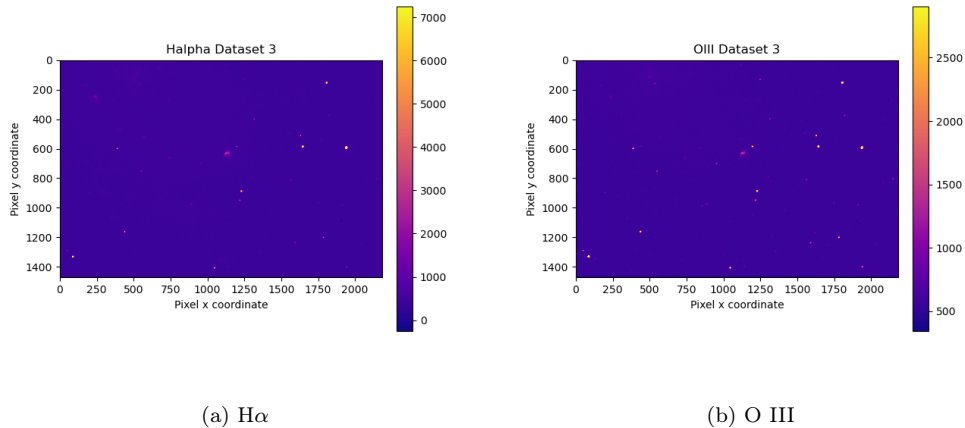


Figure 4: Calibrated science images in $H\alpha$ and $[O III]$ from October 27, 2024.

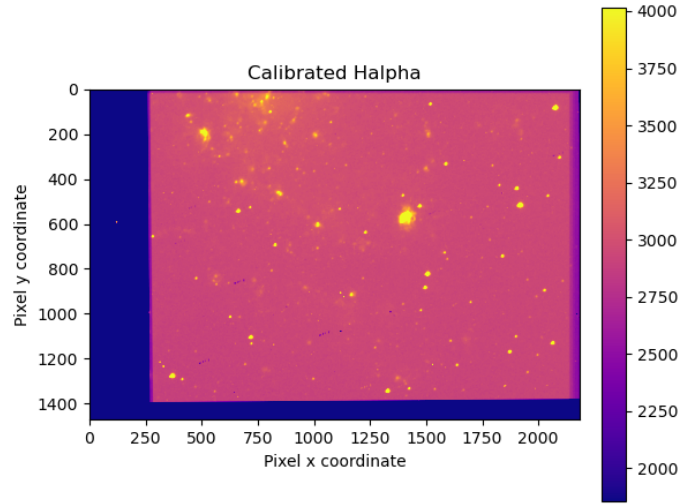


Figure 5: The calibrated $H\alpha$ science image from all datasets.

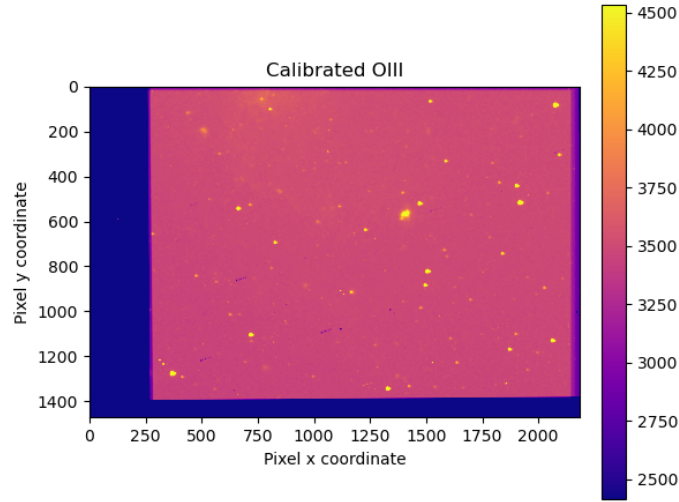


Figure 6: The calibrated $[O\ III]$ science image from all datasets.

have not received official designations are labeled with an 'N' followed by a number.

Note: We will plate solve to determine RA and DEC for the objects. This has not been done yet.

For each nebula, an elliptical sky annulus was placed and rotated to encompass the nebula and avoid including additional stars or nebulae in the target or sky background signal. We determined the photometric target aperture ellipse through size analysis, detailed below. Aperture photometry is performed using the selected apertures. Annuli for the selected nebulae are shown in Figure 7.

In particular, the brightness of the sky background in electrons (e^-) is determined by multiplying each ADU value in the sky annulus by the CCD gain in e^-/ADU and then taking the median. The uncertainty in the contribution of the sky background for each pixel, σ_s is found by taking the standard deviation of the electron counts of the pixels in the sky annulus. The uncertainty in the sky background, $\sigma_{\bar{s}}$, is σ_s divided by the square

Nebula	H α Coordinates [Pixels]	[O III] Coordinates [Pixels]	RA [h:m:s]	DEC [°: ': "]
NGC 604	[1408, 572]	[1406, 570]	01:24:33.79	+30:46:59
NGC 595	[509, 198]	[509, 198]		
N1	[1508, 190]	[1506, 201]		
N2	[960, 888]	[959, 887]		
N3	[786, 1255]	[780, 1251]		
N4	[1901, 142]	[1896, 151]		

Table 4: Analyzed Nebulae.

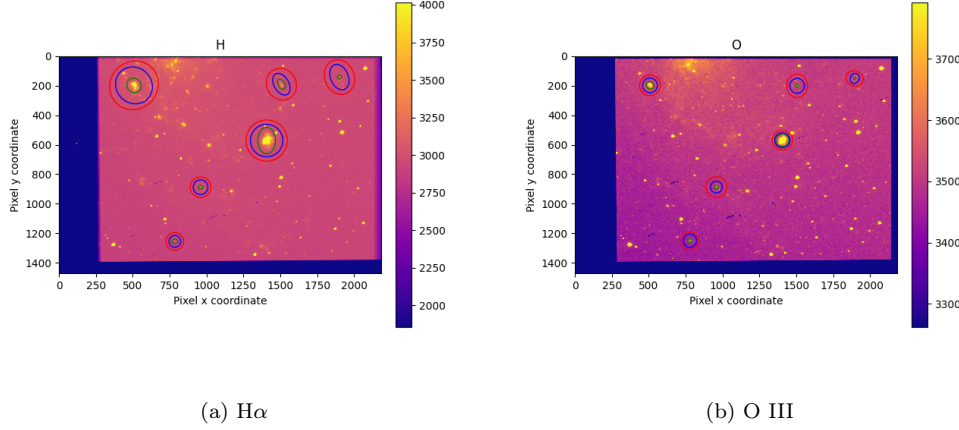


Figure 7: Annuli for photometric analysis in H α and [O III] images.

root of the number of pixels in the sky annulus.

We determined the target brightness T by converting the ADU values of pixels in the target aperture to e^- , subtracting the sky background from each pixel, and then taking the sum of all corrected pixels in the target aperture. The uncertainty in the target brightness is given by the following equation:

$$\sigma_T = \sqrt{T + N\sigma_s^2 + N\sigma_{\bar{s}}^2} \quad (2)$$

where N is the number of pixels inside the target aperture, T is the flux located inside target ellipse in e^- due to signal caused by the target nebula, σ_s is the Poisson uncertainty of the sky brightness in each pixel in e^- , and $\sigma_{\bar{s}}$ is the uncertainty in the sky brightness in e^- . To convert the target flux from electrons to photons, we then divided by the quantum efficiency of the CCD sensor we were using. For the ST-10XME, the quantum efficiency at the wavelength of the 656.3 nm H- α line is $(85 \pm 2)\%$ and the quantum efficiency at the wavelength of the 500.7nm [O III] is $(67 \pm 2)\%$.

4.3 Size Analysis

To determine the sizes of each nebula, T and σ_T were calculated iteratively with target apertures of slowly advancing semi-major and semi-minor axes, beginning at one pixel each. The semi-dimension along one axis was incremented one pixel at a time until the resulting signal increase was no longer greater than the sky background noise by 5σ . The same routine was performed along the other axis. This process is repeated until incrementing the size in either direction no longer increases the flux significantly.

Once increasing the target aperture size no longer resulted in a flux increase significantly greater than the sky background noise, the semi-major axis is defined as the larger of the two semi-dimensions and the semi-minor axis is the smaller of the two semi-dimensions. The resulting semi-major and semi-minor axes, along with the rotation angle of the target aperture, define the apparent size of the analyzed nebula in pixels. Since we are growing the target ellipse by 1 pixel each time, the uncertainty in the value of the target ellipse is given by the 1/3rd rule or 0.33 pixels. When this process was applied to NGC 604 in H α , the target ellipse included multiple bright stars and so the target ellipse was manually resized to the smallest size that excluded both stars. The

167 difference between the manual resizing and the calculated value was then added to the uncertainty given by the
 168 1/3rd rule to give upper bound.

169 5 Results

170 The brightnesses and sizes of six nebulae were analyzed. Tables 5 and 6 list the flux F and uncertainty σ_F for
 171 each nebula in $H\alpha$ and $[O\ III]$, respectively. Tables 7 and 8 list the sizes of each nebula in both filters. Nebula
 172 size is characterized by the semi-dimension along the x-axis prior to rotation (R_x) and semi-dimension along the
 173 y-axis (R_y) of an ellipse and a rotation angle θ .

Nebula	$H\alpha$ Coordinates [Pixels]	$F_{H\alpha}$ [Photons]	$\sigma_{F_{H\alpha}}$ [Photons]
NGC 604	[1408, 572]	1.32×10^7	5×10^5
NGC 595	[509, 198]	3.8×10^6	1×10^5
N1	[1508, 190]	5.0×10^5	2×10^4
N2	[960, 888]	1.18×10^5	5×10^3
N3	[786, 1255]	1.21×10^5	5×10^3
N4	[1901, 142]	1.13×10^5	5×10^3

Table 5: Nebulae brightnesses in the $H\alpha$ filter.

Nebula	$[O\ III]$ Coordinates [Pixels]	$F_{[OIII]}$ [Photons]	$\sigma_{F_{[OIII]}}$ [Photons]
NGC 604	[1406, 570]	3.5×10^6	1×10^5
NGC 595	[509, 198]	5.9×10^5	2×10^4
N1	[1506, 201]	6.2×10^4	3×10^3
N2	[959, 887]	9.7×10^4	4×10^3
N3	[780, 1251]	1.22×10^5	5×10^3
N4	[1896, 151]	2.7×10^4	2×10^3

Table 6: Nebulae brightnesses in the $[O\ III]$ filter.

Nebula	$H\alpha$ Coordinates [Pixels]	R_x [Pixels]	σ_{R_x} [Pixels]	R_y [Pixels]	σ_{R_y} [Pixels]	θ_{rot}
NGC 604	[1408, 572]	60	$+17.3, -0.3$	90	$+15.3 - 0.3$	0
NGC 595	[509, 198]	51	± 0.3	47	± 0.3	$\pi/4$
N1	[1508, 190]	22	± 0.3	38	± 0.3	$-\pi/6$
N2	[960, 888]	15	± 0.3	12	± 0.3	0
N3	[786, 1255]	20	± 0.3	16	± 0.3	0
N4	[1901, 142]	15	± 0.3	13	± 0.3	$-\pi/8$

Table 7: Nebulae sizes in the $H\alpha$ filter. R_x and R_y are the semi-dimensions of the ellipse, respectively. θ_{rot} is the clockwise rotation angle of the target aperture.

174 We calculated the area A of each ellipse and its uncertainty σ_A for each nebula:

$$A = \pi R_x R_y \quad (3)$$

$$\sigma_A = A \sqrt{\left(\frac{\sigma_{R_x}}{R_x}\right)^2 + \left(\frac{\sigma_{R_y}}{R_y}\right)^2} \quad (4)$$

176 Ellipse areas are given in Table 9.

Nebula	[O III] Coordinates [Pixels]	R_x [Pixels]	σ_{R_x} [Pixels]	R_y [Pixels]	σ_{R_y} [Pixels]	θ_{rot}
NGC 604	[1406, 570]	45	± 0.3	43	± 0.3	0
NGC 595	[509, 198]	27	± 0.3	24	± 0.3	$\pi/4$
N1	[1506, 201]	9	± 0.3	13	± 0.3	0
N2	[959, 887]	14	± 0.3	10	± 0.3	0
N3	[780, 1251]	14	± 0.3	14	± 0.3	0
N4	[1896, 151]	7	± 0.3	10	± 0.3	$\pi/8$

Table 8: Nebulae sizes in the [O III] filter. R_x and R_y are the semi-dimensions of the ellipse, respectively. θ_{rot} is the clockwise rotation angle of the target aperture.

Nebula	Coordinates [Pixels]	A [Pixels ²]	σ_A [Pixels ²]	Filter
NGC 604	[1408, 572]	16964.6	101.9	H α
NGC 604	[1406, 570]	6079.0	58.7	[O III]
NGC 595	[509, 198]	7530.4	65.4	H α
NGC 595	[509, 198]	2035.8	34.0	[O III]
N1	[1508, 190]	2626.4	41.4	H α
N1	[1506, 201]	367.6	14.9	[O III]
N2	[960, 888]	565.5	18.1	H α
N2	[959, 887]	439.8	16.2	[O III]
N3	[786, 1255]	1005.3	24.1	H α
N3	[780, 1251]	615.8	18.7	[O III]
N4	[1901, 142]	612.6	18.7	H α
N4	[1896, 151]	219.9	11.5	[O III]

Table 9: Ellipse areas as a measure of nebula size.

Finally, the ratios of fluxes (ϕ_F) and areas (ϕ_A) and their uncertainties (σ_{ϕ_F} and σ_{ϕ_A} , respectively) between the two filters were calculated for each nebula. For example,

$$\phi_F = \frac{F_{H\alpha}}{F_{[OIII]}} \quad (5)$$

$$\sigma_{\phi_F} = \phi_F \sqrt{\left(\frac{\sigma_{F_{H\alpha}}}{F_{H\alpha}}\right)^2 + \left(\frac{\sigma_{F_{[OIII]}}}{F_{[OIII]}}\right)^2} \quad (6)$$

Ratios and their uncertainties are given in Table 10.

Nebula	H α Coordinates [Pixels]	ϕ_F	σ_{ϕ_F}	ϕ_A	σ_{ϕ_A}
NGC 604	[1408, 572]	3.50	0.17	2.79	0.03
NGC 595	[509, 198]	6.49	0.32	3.70	0.07
N1	[1508, 190]	8.13	0.51	7.15	0.31
N2	[960, 888]	1.22	0.07	1.29	0.06
N3	[786, 1255]	0.99	0.06	1.63	0.06
N4	[1901, 142]	4.16	0.37	2.79	0.17

Table 10: Ratio of flux and ellipse area between H α and [O III] for each nebula.

The average ratio of nebula flux in H α to flux in [O III] is 4.08 ± 0.12 . The average ratio of nebula area in H α to flux in [O III] is 3.22 ± 0.06 . Uncertainties in averages were obtained by propagating errors in the individual quantities, as in, for instance:

$$\sigma_{\phi_F} = \sqrt{\sum_i \left(\frac{\sigma_{\phi_F,i}}{N} \right)^2} \quad (7)$$

where σ_{ϕ_F} is the uncertainty in the average flux ratio, $\sigma_{\phi_F,i}$ is the uncertainty in a given nebula flux ratio, and N is the number of flux ratios averaged. The same equation applies for the ellipse area ratio.

6 Discussion

Based on the emission nebulae analyzed, HII regions in M33 typically appear brighter and larger in $H\alpha$ than in [O III], in agreement with our initial hypothesis. As Table 10 shows, all analyzed nebulae exhibit $H\alpha$ to [O III] flux and area ratios greater than or equal to 1 within uncertainties. We therefore reject the null hypothesis that there is no systematic difference between $H\alpha$ and [O III] emissions from HII regions in M33. This result indicates that some physical processes in M33's emission nebulae give rise to brighter $H\alpha$ emissions in a larger area.

Some of the factors discussed in the introduction may lead to the significantly stronger $H\alpha$ emissions than [O III] emissions, such as the greater abundance of ionized hydrogen in HII regions, the larger energy input required to produce [O III] recombination emission (localizing [O III] emissions to regions near ultraviolet-emitting sources), and more dispersion of atomic hydrogen by stellar winds. NGC 604 is 3.50 ± 0.17 times brighter and 2.79 ± 0.03 times larger in $H\alpha$ than in [O III] – similar factors to the overall average among all analyzed nebulae: 4.08 ± 0.12 times brighter and 3.22 ± 0.06 times larger in the $H\alpha$ filter than in [O III]. This suggests that the physical processes occurring in NGC 604 are similar to those in other star-forming HII regions in its local area of M33.

By imaging more portions of M33, additional emission nebulae can be analyzed, providing a more robust understanding of M33 in the $H\alpha$ and [O III] narrowband filters. With additional information about the University of Maryland, College Park Observatory telescopes an instrumental magnitude and apparent magnitude for each nebula can be determined to create a comprehensive catalog of emission nebulae in M33. Such a catalog, through further study, would allow us to enhance our understanding of HII regions, M33's formation, and the nature of the atomic hydrogen bridge between M33 and M31, including its role as a progenitor of star-forming regions.

NOTE: We plan to analyze additional nebulae available in our images. Additionally, we may perform a more comprehensive statistical analysis on the differences between regions beyond the average of the ratios.

7 Acknowledgments

Some suggestions for revising the Introduction from ChatGPT4-mini.

8 Bibliography

References

- Bekki, K. 2008, Monthly Notices of the Royal Astronomical Society: Letters, 390, doi: 10.1111/j.1745-3933.2008.00528.x
- Eldridge, J. J., & Relaño, M. 2011, , 411, 235, doi: 10.1111/j.1365-2966.2010.17676.x
- Freedman, R. A., Geller, R., & Kaufmann, W. J. 2019, Universe, 11th Edition (Macmillan)
- Hodge, P. W., Balsley, J., Wyder, T. K., & Skelton, B. P. 1999, The Astronomical Society of the Pacific, 111, doi: 10.1086/316374
- Nilson, P. 1973, Nova Acta Regiae Soc. Sci. Upsaliensis Ser. V, 0
- Pettit, E. 1954, The Astrophysical Journal, 120, doi: 10.1086/145932
- Tabatabaei, F. S., Cotton, W., Schinnerer, E., et al. 2022, , 517, 2990, doi: 10.1093/mnras/stac2514
- Thilker, D. A., Braun, R., Walterbos, R. A. M., et al. 2004, The Astrophysical Journal, 601, 39, doi: 10.1086/381703